*J. Fluid Mech.* (1989), *vol.* 202, *pp.* 467–497
*Printed in Great Britain*



# Droplet pair interactions in a shock-wave flow field

By S. TEMKIN AND G. Z. ECKER†
Department of Mechanical and Aerospace Engineering, Rutgers University, New Brunswick, N.J. 08854, USA

(Received 25 March 1988)

Binary interactions between water droplets of nearly equal size in the flow field behind a weak shock wave were studied experimentally. The droplets had diameters of about 270 mm, and the Reynolds numbers, based on this diameter and on the relative velocity between the droplets and the free stream, ranged from about 130 to about 600. In this paper we report only data for $Re < 150$, corresponding to non-deforming droplets. The droplets in a given pair were aligned so that each pair fell on a plane parallel to the direction of the incoming flow. In this manner, the second droplet in the pair was 'behind' the first, at horizontal distances ranging from 1.5 to 11 diameters, and at vertical distances from the dividing streamline ranging from $-3$ to 6 diameters. We have quantified the interaction in terms of drag force changes on the droplets, and show that the first, or upstream, droplet is not affected by the second, but that the second experiences significant reductions for vertical distances of about one droplet diameter or less. At the smallest horizontal distances, the maximum decrease observed was about 50%, relative to its isolated value. We also show that the drag changes clearly demarcate a wake behind the first droplet. Further, on the basis of these changes, we define a region of influence attached to the first droplet, where the free-stream velocity is significantly reduced. For the droplets used in this study, this region is a slender paraboloid of revolution, having a length of about 15 diameters and a radius of about one diameter.

## 1. Introduction

In this paper, we report results of an experimental investigation on the interaction between droplet pairs in a transient flow field produced by the passage of relatively weak shock waves. The work was motivated by earlier experimental work, which showed that a weak shock wave travelling in a liquid-droplet aerosol cloud can induce collision and coalescence (Temkin, 1970). The possibility that those effects were in part produced by fluid forces on the droplets which, owing to the highly unsteady nature of the interaction, might be significantly different from their steady values, induced us to investigate the shock wave–droplet interaction in some detail for the case of both deforming and non-deforming droplets (Temkin 1972; Reichman & Temkin 1974; Temkin & Kim 1980; Temkin & Metha 1982). Also investigated was the related phenomenon of electrical charge separation due to droplet breakup (Dreyfuss & Temkin 1983). While these works shed some light on the interaction, particularly in regard to the drag in unsteady conditions, the reasons for the earlier observations of coalescence remained unknown. It therefore became evident that in order to understand the effects resulting in the observed coalescence, it would be necessary to perform the significantly more difficult experiment of observing

† Present address: Ministry of Defense, Haifa, Israel.

interactions as a droplet pair responds to the passage of a shock wave. The experiments were conducted with parallel and coplanar stream of droplets, rather than with an aerosol cloud. Because of this arrangement, the sought reason for the earlier observations were quickly identified. This is simply the transient wake that is produced in the lee side of one droplet, due to the passage of the wave. If a second droplet is in the vicinity of this wake, it will experience smaller fluid forces than the first. The first droplet may therefore move much more rapidly than the second, possibly producing a collision.

This retardation effect is, of course, basically the same as that produced by the wakes of cars and trucks on a road. In retrospect, this transient wake effect taking place owing to the passage of shock waves might have been anticipated earlier, as it no doubt plays some role in at least two areas of current interest. One is acoustic coagulation of particulates (solid or liquid), where an aerosol cloud is exposed to the effects of intense acoustic waves. The second area is cloud physics, where a wake effect producing gravitational coalescence was identified some time ago (Woods 1964), but where the possibility that thunderclaps may also produce coalescence by a wake effect has not been considered, even though thunder has been mentioned as a possible coalescence-producing mechanism (Goyer 1965*a*,*b*; Temkin 1969).

Here we first give some qualitive evidence of the wake that is formed behind a droplet, and of the collisions that sometimes result due to it. The bulk of the results presented here are quantitative measurements of the interaction between droplet pairs of approximately equal size, which are not colliding during the observations. The interactions are measured in terms of the changes of the drag coefficient of the second droplet in the droplet pair, relative to the single-droplet drag. These results were obtained with droplet pairs initially separated by distances along the direction of the flow varying between 2 and 11 droplet diameters (270 μm), and exposed to flow fields having velocities in the range 680 to 3100 cm/s. The corresponding initial Reynolds number $Re$, based on the diameter of the first droplet and on the flow velocity, ranged from 130 to 600. The data reported here are limited to $Re < 150$, for which no deformation takes place. This limit is necessary because this work requires accurate drag coefficients for single droplets, and these are not available for deforming droplets.

The results show that the second droplet can experience reductions in the drag coefficients as high as 50% relative to its independent drag. This reduction occurs at the smallest separation distances used and for droplets that are instantaneously aligned with the dividing streamline behind the first droplet. For other separations and distances from that streamline, drag reductions decrease. The decrease with distance from the dividing streamline is very rapid, becoming negligible at distances of the order of one droplet diameter. For a given distance to the dividing streamline, the drag reduction decreases slowly with the horizontal distance between the droplets. A main result is that the drag-reduction curve appears to be well described by log normal distributions, whose maximum value depends on the initial horizontal separation. Further, by a suitable choice of parameters, the different distributions can be made to collapse onto a single curve. These results can therefore be used to quantify the region behind the first droplet where significant interaction takes place. This drag-reduction region gives a good idea of the wake that is formed behind a droplet after the passage of a shock wave. This information may be useful in quantifying droplet interactions in a variety of situations.

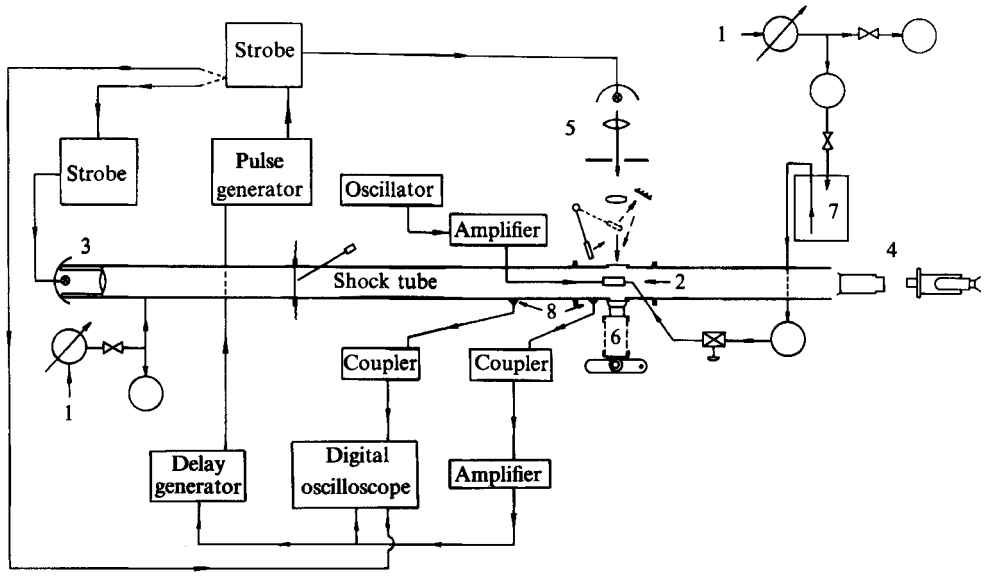


FIGURE 1. Experimental facility: 1 pressurized air; 2 droplet generator; 3 axial illumination system; 4 axial alignment system; 5 transverse illumination system; 6 camera for transverse photographs; 7 water supply; 8 pressure transducers.

## 2. Experimental apparatus

The experimental set-up is schematically shown in figure 1. It consists of a horizontal shock tube capable of producing controlled shock waves of weak strength, a droplet generator which produces parallel and coplanar streams of nearly equal-sized droplets, and optical set-ups that can be used to produce photographic records of the droplet pairs as they move in the flow. These main components as well as the electronic equipment associated with them are described below. Considerably more detailed descriptions of these components can be found elsewhere (Ecker 1985).

### 2.1. *Shock tube*

The experiments were conducted in an existing horizontal shock tube that had been used in some of our previous work. Except for the modifications mentioned below, the main features of the tube are as described earlier (Temkin & Kim 1980). The modifications include a new test section, a more rigid structure supporting the tube, and a change in the driver section that permits the place of a stroboscopic lamp needed for visual observations of the droplets from the open end of the driven portion of the tube. A particularly important change for this work was a very careful alignment of the whole tube that ensures that it is levelled within 1° from the horizontal, and that its axis is aligned within 5 mm along its 5500 mm length. This high degree of accuracy is needed to ensure that the droplet pairs are falling on a plane that contains the axis of the tube.

A typical pressure record during one experiment is shown in figure 2. It shows the rapid pressure rise associated with the arrival of the shock front, followed by a region in which the pressure changes slightly and then by a region of constant pressure. The small difference between these two regions, usually less than 3% of the maximum value of the pressure increase, is due to expansion waves that emanate from the ports

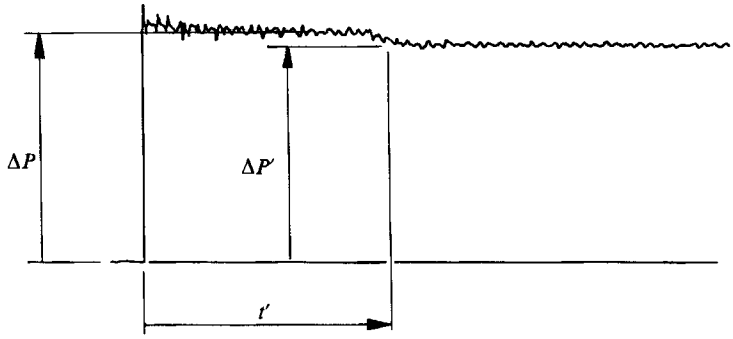


FIGURE 2. Typical pressure record.

in the test-section window, where the droplets enter and leave that section. Their duration $t'$ as indicated in the figure, corresponding to the transit time of those waves, and is of the order of 2 ms. The total test time is of the order of 10 ms.

### 2.2 *Droplet-pair generator*

As in our past work with droplets, we used the well-known capillary instability of thin jets to produce droplets of controlled size and separation. However, because of the requirements for the present investigation, a new design had to be used. Basically, the work required that droplet pairs of nearly equal size be produced that in the absence of any flow could be allowed to fall across the shock tube, along parallel trajectories. This simple requirement presented considerable difficulties, as explained below.

The new droplet generator system is schematically shown in figure 3. Highly purified water†, produced separately, is placed in a 1 gallon container, which is then pressurized to a nominal pressure of 60 mm Hg. The water flowing out of the container passes through a 0.22 μm Millipore filter which provides additional filtering for suspended particulate matter that may be present. It then passes through a micrometric needle valve. Although the valve produces very accurate control of the flow rate, its main purpose is to provide very steady flow rates, which are essential for the production of droplets (typical flow rates of the order of 2–4 cc/min). The water then enters a chamber in the generator where an acoustic disturbance, produced by a piezoelectric transducer is imposed on it before it exits the generator, in the form of two thin jets, through pinholes made by a laser in thin disks located at the bottom of the generator. If the frequency and amplitude of the disturbance are suitably chosen, the jets will break up into streams of equally sized droplets.

The transducers used consist of thin piezoelectric disks bonded to stainless steel supporting plates, and mounted in the generator so that they can be forced to vibrate easily. In earlier designs, the disturbance was introduced by means of a bimetal, cantilever-shaped, transducer immersed in the water, This immersion prevented it from vibrating easily. The current design provides a considerably more efficient transduction, and prevents corrosion of the metal plate supporting the ceramic

† The water used in this research meets the specification II of the College of American Pathologists, which requires that the resistivity be greater than 2 MΩ−cm. Our water, produced by processing tap water through a Barnstead D8922 type combination cartridge, had a resistivity of 10 MΩ−cm. One reason for using such a high degree of purity was to eliminate variations of the surface-tension coefficient.

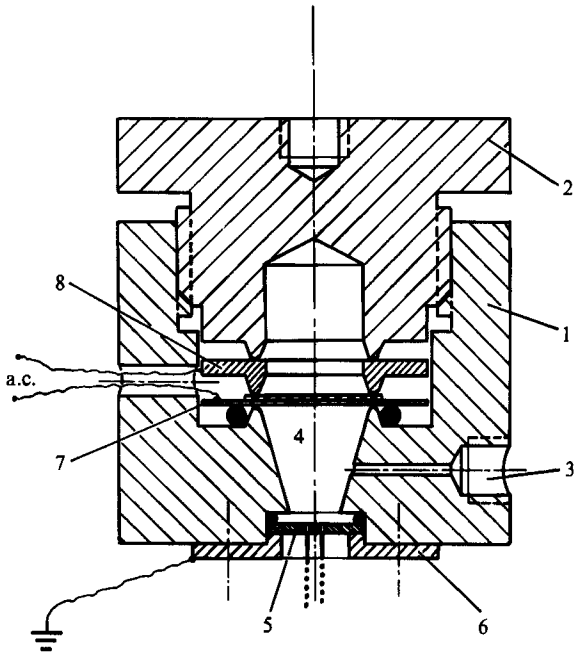


FIGURE 3. Droplet generator: 1 main body; 2 cap; 3 water inlet; 4 acoustic chamber; 5 double pinhole disk; 6 brass holder; 7 piezoelectric transducer; 8 brass contact plate.

transducer. It also permits several transducer diameters to be used, which broadens the range of available excitation frequencies.

In order to produce droplet pairs, we initially designed and tested two different types of exit plates, one with parallel hypodermic needles, and one with pinholes. Although some success was obtained with parallel needles, that design was abandoned as the droplets produced with it were too large for our purposes. On the other hand, the double pinhole design proved capable of producing considerably smaller droplets, although it required considerable effort and ingenuity to produce the required streams. The main difficulty was that the jets issuing from laser-produced pinholes were less coplanar and parallel than this experiment requires. Thus, for example, we required that the droplets deviated from a vertical plane by less that 5% of their diameter in the 15 mm travel distance across the test-section window. For a 300 μm droplet this meant a tolerance of 1 milliradian. When the pinholes were tested, it was observed that all of them produced streams exceeding the required tolerances. A microscopic inspection of the pinholes' inner surface, revealed the they were not cylindrical, as initially anticipated†. It was also observed that the water jets deviated by larger angles from the vertical when emerging through the side designated as 'inlet' in figure 4. Further, small disturbances, such as a small change of the flow rate would often result in a different exit angle. We attributed this behaviour to the curvature of the pinhole's exit profile. That is, as the water moves into the pinhole, a minimum jet diameter is formed near the throat of the pinhole, but necessarily separates from part of the internal contour as it emerges,

† The cross-sectional profiles shown by the pinhole orifices are an inherent characteristic of laser-made orifices. They are produced by the focusing of the beam that is needed to make the perforations.

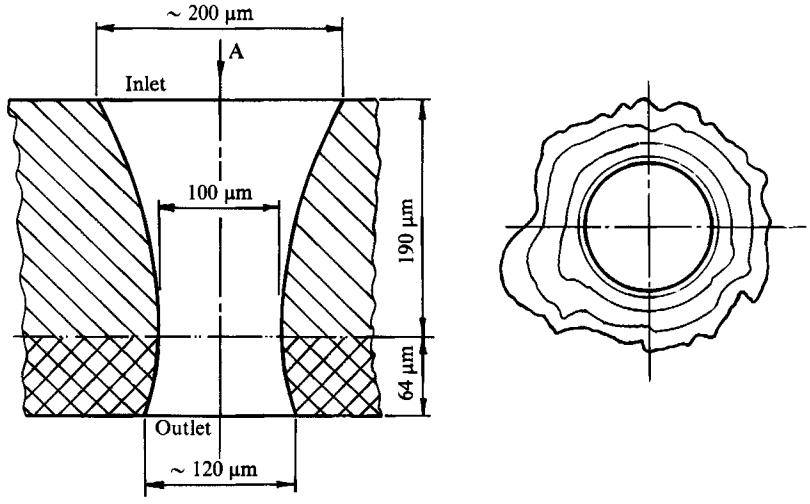


FIGURE 4. Cross-section through pinhole.

with the point of separation, and therefore the angle of attachment, not remaining stable.

To improve the performance of the device, the exit cones of the pinholes were eliminated by grinding 64 μm off each surface. This eliminated the noted instabilities in two of our pinhole disks. Most of the experimental work was conducted with streams produced by these disks. They had pinhole diameters equal to 102.3 and 92.1 μm, separated by distances of 410.2 and 1207.8 μm, respectively. The 102.3 μm diameter pinhole is referred to as the 'first' pinhole in this work. The label 'first' is used to denote the pinhole on the 'upstream' side, that is, droplets produced by this orifice are exposed to the incoming flow earlier than those produced by the second. It is seen that the diameter of the first pinhole was about 10% larger than that of the second. This difference, as well as the location relative the flow, was intended to produce droplets pairs having nearly equal diameters, but with the slightly larger droplet exposed first to the imposed transient flow. This requirement was imposed by a separate study of shock-induced collisions between nearly equal-sized droplet pairs, in which it was desirable to avoid collisions produced purely by size effects, such as might be produced if the smaller droplet were exposed to the incoming flow before the larger droplet. Of course, if needed, small–large droplet pairs could be used by simple rotation of the disk. We did not study such pairs. Figure 5 shows examples of parallel stream of droplets from one of the pinholes produced in the above manner. Table 1 gives the values of the frequencies, droplet diameters and other parameters corresponding to these streams. (The characteristics of the droplet streams used in our interaction experiments are given by Ecker 1985. They were obtained with an oscillator frequency in the vicinity of 2000 Hz, as this frequency band produced a high degree of stability during long periods of time.) The ratios $s/D$ give the vertical distances between droplets in the respective streams. These quantities could be varied within a limited range, as demonstrated by figure 5, but except for runs 30/11 and 30/12, they had similar values for both streams. Within each stream, the droplets have slightly different diameters and distances, but the differences are very small, as shown in Appendix A, where data on streams used in one of our interaction experiments are given. Because of this, we reduced the motion data using average values for a given stream.

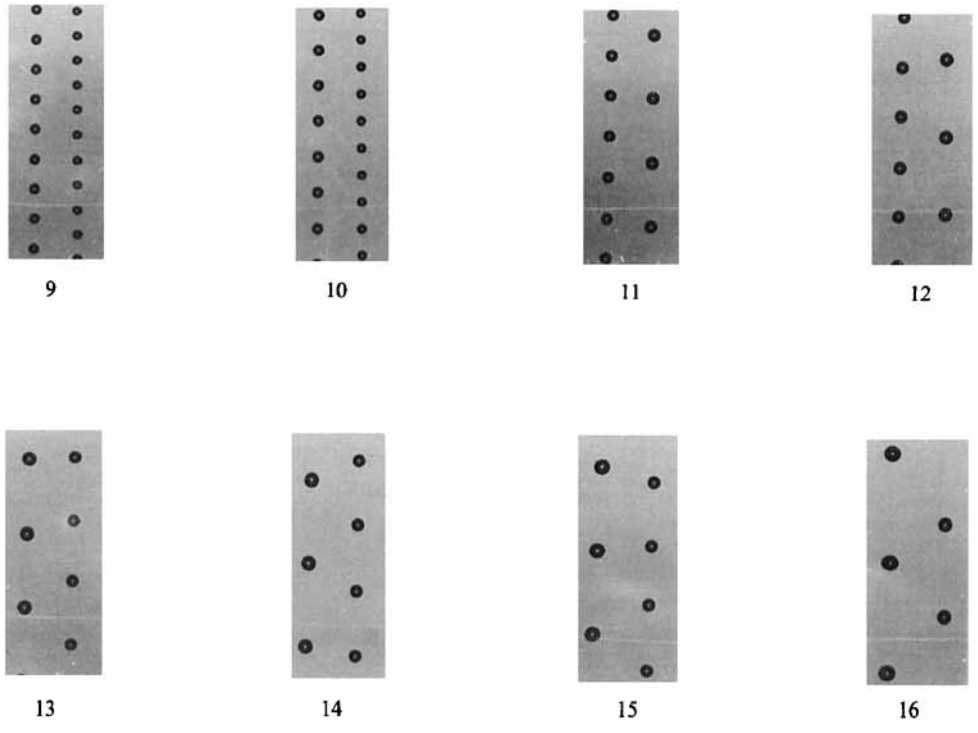


FIGURE 5. Examples of droplet streams.

| Test no. | $d_0$(μm) | $f$(HZ) | $D$(μm) | $s$(μm) | $s/D$ |
|---|---|---|---|---|---|
| 30/09 | 102.3 | 4350 | 219 | 670.1 | 3.1 |
| 30/09 | 92.1 | 4350 | 191 | 548.2 | 2.9 |
| 30/10 | 102.3 | 3750 | 237 | 848.5 | 3.6 |
| 30/10 | 92.1 | 3750 | 201 | 639.2 | 3.2 |
| 30/11 | 102.3 | 3200 | 248 | 972.2 | 3.9 |
| 30/11 | 92.1 | 3200 | 264 | 1446.7 | 5.5 |
| 30/12 | 102.3 | 2800 | 264 | 1172.2 | 4.4 |
| 30/12 | 92.1 | 2800 | 283 | 1780.1 | 6.3 |
| 30/13 | 102.3 | 2020 | 292 | 1585.6 | 5.4 |
| 30/13 | 92.1 | 2020 | 252 | 1257.5 | 5.0 |
| 30/14 | 102.3 | 1880 | 301 | 1736.8 | 5.8 |
| 30/14 | 92.1 | 1880 | 261 | 1396.4 | 5.4 |
| 30/15 | 102.3 | 1470 | 309 | 1878.7 | 6.1 |
| 30/15 | 92.1 | 1470 | 265 | 1462.8 | 5.5 |
| 30/16 | 102.3 | 1150 | 336 | 2415.8 | 7.2 |
| 30/16 | 92.1 | 1150 | 291 | 1938.1 | 6.7 |

TABLE 1. Characteristics of the droplet streams shown in figure 5

### 2.3. *Droplet illumination and photography*

Three types of schemes were used to provide illumination for droplet pair photography. All of them required controlled stroboscopic sources, which could be triggered when desired, delayed by stipulated times, accurate to within a

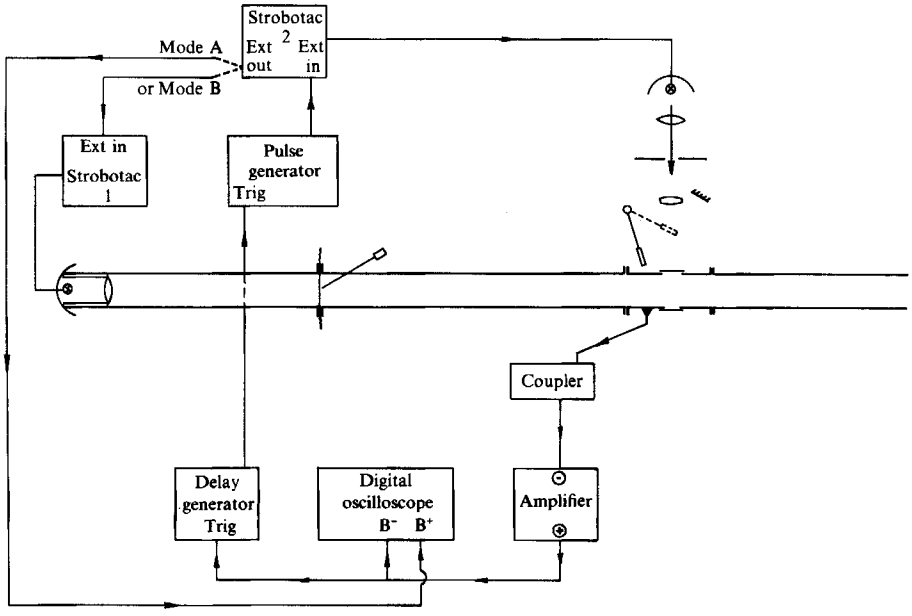


FIGURE 6. Electronic components for the illumination system.

microsecond, and producing a variable number of flashes as desired. Two of the illumination schemes involved optical beams perpendicular to the axis of the tube. The third involved a beam along the axis of the tube. The electronic components required for the three beams are shown in figure 6. The transverse arrangement is schematically shown in figure 7. It uses a Koehler-type illumination which provides a uniform beam in the test section whose intensity can be controlled by an iris diaphragm. Depending on the position of a mirror, the beam can be used to produce two types of illumination. In one, the beam crosses the test section at an angle with respect to the plane upon which the droplets move. It is therefore suitable for scattered-light photography, of the type shown in figure 8. In the second, the beam crosses the test section in a direction perpendicular to the axis of the tube. As such, it is suitable for back-lighted photography, such as shown in figure 5, or for obtaining shadowgraphs across the tube. The receiving optical system is the same for both illuminating systems. It consists of a 55 mm Macro Nikkor lens, bellows, and a 35 mm Nikon camera. The lens is mounted on the bellows in its reverse position, in order to provide a suitable working distance to the droplets. Optical magnifications were carefully calibrated for the range of magnifications used.

The purpose of the transverse system was to measure the diameter of the droplets, and to record on a negative the positions of the droplets as they moved in response to the incoming flow. The photographic negatives obtained are analysed with a Bausch & Lomb Contour Projector that has an X–Y micrometric table with 2 μm divisions. The unit is used with a 10X magnifying lens in the case of bright field illumination, and with a 50X magnifying lens for the examination of scattered-light, or dark-field illumination negatives. Because of the low intensity of the scattered light, and because of the 2–3 times magnifications used by the receiving transverse system, it was found necessary to use Kodak 2475 Recording film. This has a nominal speed of 1250 ASA, which proved to be adequate for both scattered and direct illumination purposes.

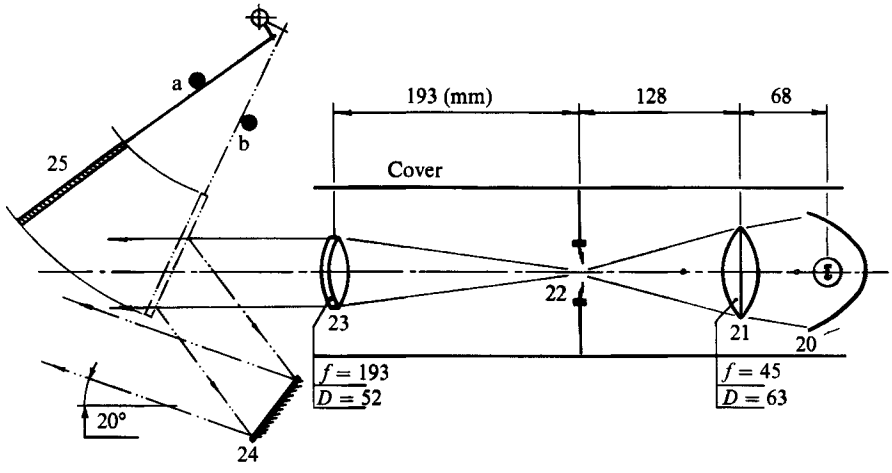


FIGURE 7. Transverse illumination system.

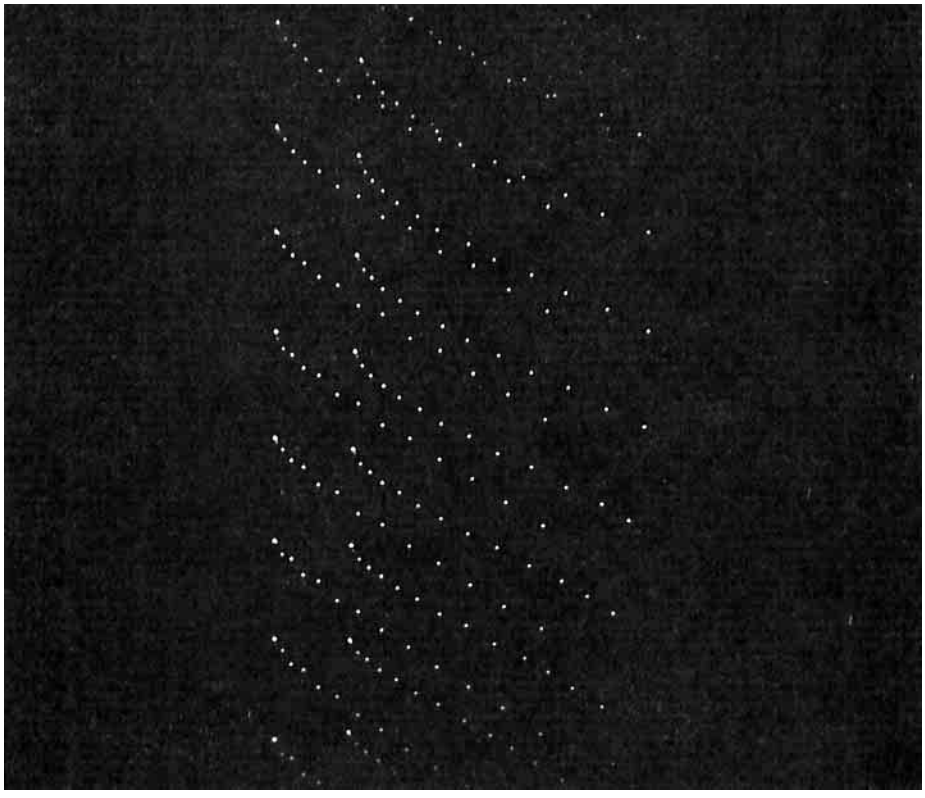

FIGURE 8. Example of scattered-light photography.

The longitudinal system uses a stroboscopic lamp and a collimating lens installed at the end of the shock-tube driver section, as shown in figure 9. The system is completed by a receiving system located at the other end of the tube, or 550 cm away. The system could be tested prior to each run, to ensure that the optical axis and the axis of the tube coincided within one milliradian. This was accomplished by

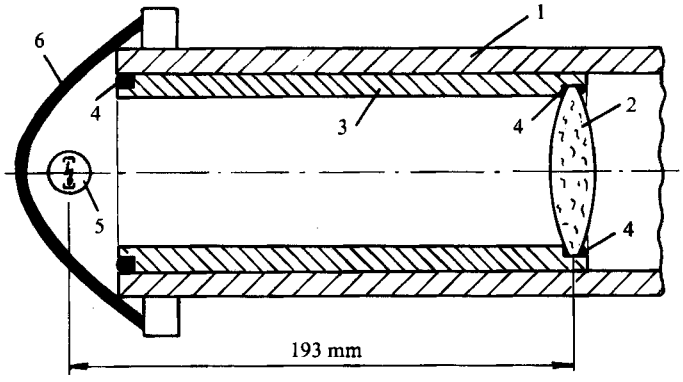


FIGURE 9. Light source for axial system: 1 shock-tube driver section; 2 lens, $fl = 193$ mm; 3 Plexiglas housing; 4 seals; 5 strobe lamp; 6 parabolic reflector.

focusing the receiving lens system alternately on two carefully centred targets; one in the test section, the other on the centre of the collimating lens in the driver section of the tube, located at about 350 cm from the centre of the test section.

During most of this study, the receiving system consisted of a 200 mm Leitz lens and an enlarging microscope. The arrangement enabled us to look at droplets from a distance equal to about 10000 droplet diameters away, for the purpose of aligning the droplet streams. In the last portion of the study, a Questar QM-1 lens was acquired, and this simplified the axial alignment considerably. Figure 10 includes two photographs, taken with the Questar lens, showing both axially misaligned and aligned droplet streams falling through the test section. Observation of the two droplet streams from the end of the stock tube thus enabled us to ensure that the droplets were on the same plane, and that this plane was parallel to the axis of the tube.

### 2.4 *Flash triggering and timing*

Because of the basic nature of the data gathered in this investigation – horizontal and vertical displacement of the droplets as a function of time – the ability to trigger a required number of flashes, starting at a precisely determined instant, and at accurately known intervals, is of paramount importance. These requirements were met with the electronic components shown in figure 1. The sequence of events triggering the flashes begins when the shock wave passes over the first pressure transducer, 8. The signal from this transducer is used to trigger the digital oscilloscope. The flash triggering system is activated when the shock reaches the second pressure transducer. This is located 75.5 mm upstream of the axis of the droplet port, and produces a signal which is first amplified, and then delayed by a suitable amount in a delay generator, so that the first flash occurs just prior to the arrival of the shock to the first droplet stream.

After being delayed, the triggering signal is fed into a pulse generator (Hewlett Packard Model 8011A), capable of generating a preset number of pulses having a preset interval between them. The pulses are then sent to one of the two stroboscopes used. Almost simultaneously with the production of each desired flash, the selected stroboscope produces a signal that is sent to the digital oscilloscope. Figure 11 shows a typical trace of the two-channel oscilloscope. Channel A shows the pressure variations at the location of the first transducer, from a time prior to the arrival there of the shock wave. Channel B shows two different signals. The first, shown as a rapid

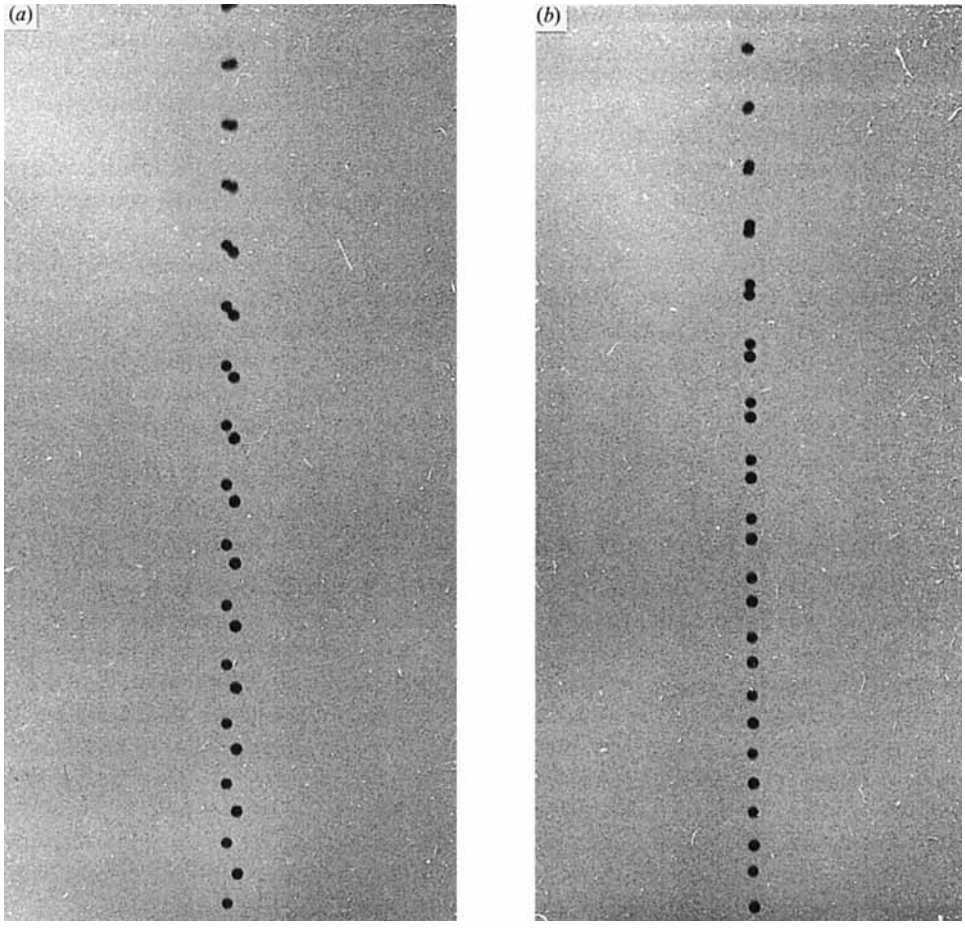


FIGURE 10. Axial photographs of droplet streams: (*a*) misaligned streams; (*b*) aligned streams.

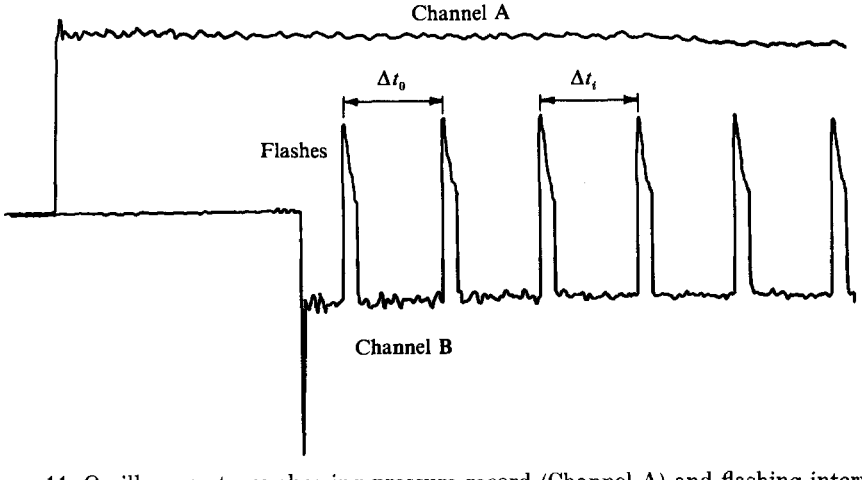


FIGURE 11. Oscilloscope trace showing pressure record (Channel A) and flashing intervals (Channel B).

change of negative polarity, is the output of the second pressure transducer, located 75.5 mm upstream of the droplet ports. The second is the external output of the stroboscope, which has been delayed by a certain amount. This second signal is shown as a sequence of positive peaks; the first one occurring sometime after the arrival of the negative polarity pulse.

The system was also carefully tested to verify that the stroboscopic lamp produced the desired number of flashes, and that the flashing interval was as selected. This tests are important because of the finite amount of time required to recharge the lamp's capacitors. In fact, as shown in the dark-field photographs, the first flash is always the most intense, the second the weakest, with the rest having uniform intensity. Also, as implied in figure 11, the time intervals between the first and second flashes, $\Delta t_0$, is different from the subsequent intervals, the difference being about 12 μs. This difference is of some help in identifying droplet streams in photographs such as those shown in figure 8. As described in the next sections, such photographs contain the basic data needed for this investigation.

## 3. Identification of interaction mechanism

Although our earlier (Temkin 1970) experiments clearly indicated that droplet pairs must strongly interact in some manner, that manner was not apparent prior to the initiation of this experiment. Thus, we did not know *a priori* what measurements, if any, could be made that would show the interaction, nor did we known how to quantify it. It was, however, evident that if we could follow the motion of a droplet in a given pair during an experiment, the interaction might affect its motion relative to its non-interacting state. We therefore determined that droplet trajectories, as revealed by instantaneous positions would be needed.

These positions were obtained from dark-field photographs, of the type shown in figure 8, where they are represented by the bright dots on the negatives. These bright dots are due to light scattered by the droplets, and their location relative to the centre of a given droplet does not change during the tests, at least for non-deforming droplets such as those used in obtaining the data reported in this article. (For deforming, but not breaking, droplets, these dots oscillate in time with a period that is considerable smaller than the time of observation. They therefore represent average values.)

To give an idea of the trajectories followed by droplet pairs, we show in figure 12, a positive print made from a dark-field photograph, for a case when the imposed flow velocity was large enough to induce the collisions referred to in the introduction. The photograph shows the trajectories followed by two pairs, with one of them colliding after some time. A black circle has been added at the initial positions of the four droplets involved, to give an idea of the size of the droplets, relative to the spots. It should be noted that the trajectories do not always coincide with those that a casual glance might indicate. These visually presumed trajectories may be an optical illusion. Actual trajectories can only be drawn by properly identifying at different times a given droplet. This most important requirement to this research was satisfied by applying the following rules to every experiment: the first flash is the strongest. This enables us to identify the streams initially; the second flash is the weakest. This enables us to identify the next position, after $t_1$, of any droplet in the stream; dots that appear at $t_2$ between the initial positions of the first and second streams can only belong to droplets in the first stream; the vertical velocity of the droplets remains nearly constant during the experiments, and can be estimated from the frequency of

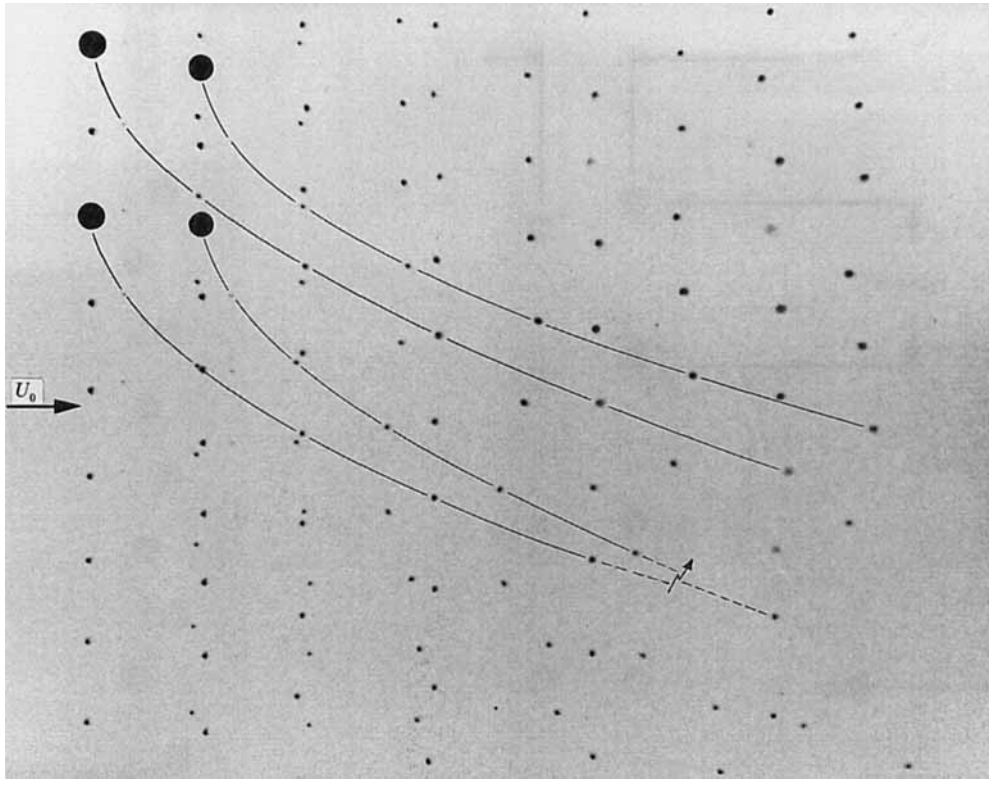


FIGURE 12. Scattered-light photograph showing trajectories of two droplet pairs.

the droplet generator and the vertical spacing; the vertical spacing between any two droplets, although slightly different for any two consecutive droplets, remains constant; finally, the droplets in the 'first' stream remain vertically aligned, while those in the second do not (and the reason for this is the interaction between the two droplets which is reported here).

Evidence for the last statement is given in figure 13, which shows two photographs of two droplet streams. In (*a*), there is no imposed flow field, so that the droplets are simply falling across the shock tube. In (*b*), taken 6.5 ms after the passage of the shock front, both streams have moved in the direction of the flow. However, we can clearly see that the first stream remains vertically aligned, but that the second stream has lost its initial alignment. Incidentally, droplet collisions induced in this manner are observed to occur even at these small velocities, but at later times, or at earlier times with larger imposed velocities, and figure 14 shows examples of such collisions.

A different manner of illustrating the interaction between the droplets in a given pair is by plotting the motion of the droplet in the second stream, relative to the droplet in the first, that is, in a frame of reference in which the first droplet is at rest. Because the droplets in the second stream are smaller that those in the first stream, their falling velocity is smaller. Therefore, relative to the first stream, the droplets in the second stream are moving upward, as shown in figure 15. We show two of the cases we have observed. In case (*a*), referred to as *trapped*, the second droplet moves up and directly into the first droplet. This is the colliding case shown in figure 14. In

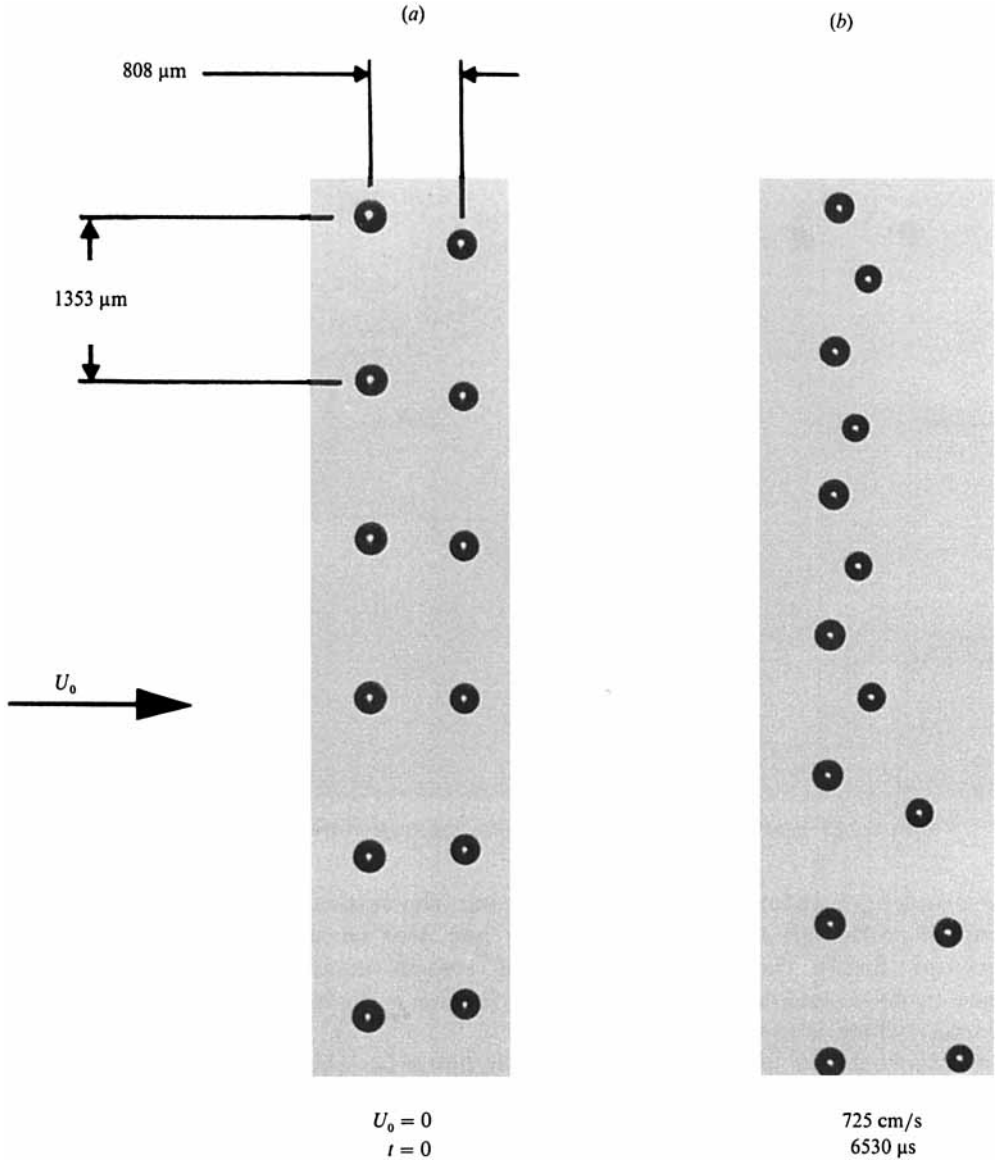


FIGURE 13. Non-deforming droplet streams before and during an experiment. (*a*) Streams before passage of shock wave. (*b*) Streams 6.53 ms after passage of wave. $Re = 140$; $We = 0.14$.

case (*b*), referred as *escaped*, the second droplet starts below the first, and ends above it, while its horizontal distance is not greatly changed. This case is the non-colliding-trajectory case shown in figure 13. A third case, called *retarded*, was also observed in which the second droplet is somewhat affected by the first, although not as drastically as in case (*a*). In the case shown, the second droplet was initially well below the wake, and had gained a sufficiently high momentum which enabled it to cross the wake with only a slight retardation.

On the basis of such results, it becomes obvious that the reason for the strong interactions observed earlier was a wake formed behind the first droplet. The situation is schematically shown in figure 16, which shows conceptual wakes as

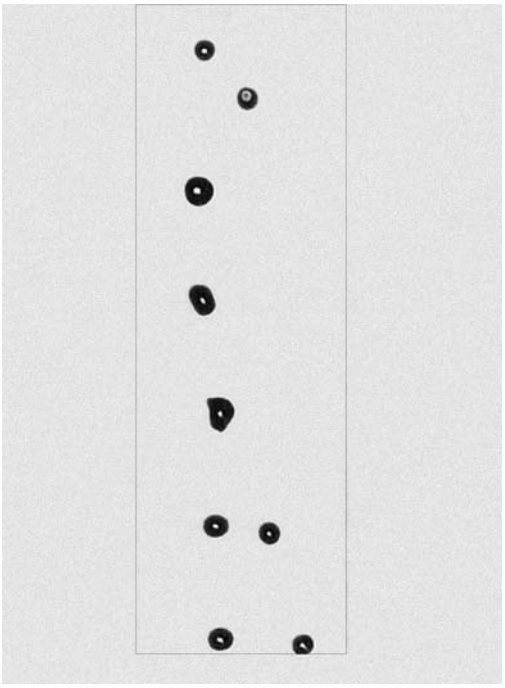

FIGURE 14. Example of droplet collisions at $Re = 380$.

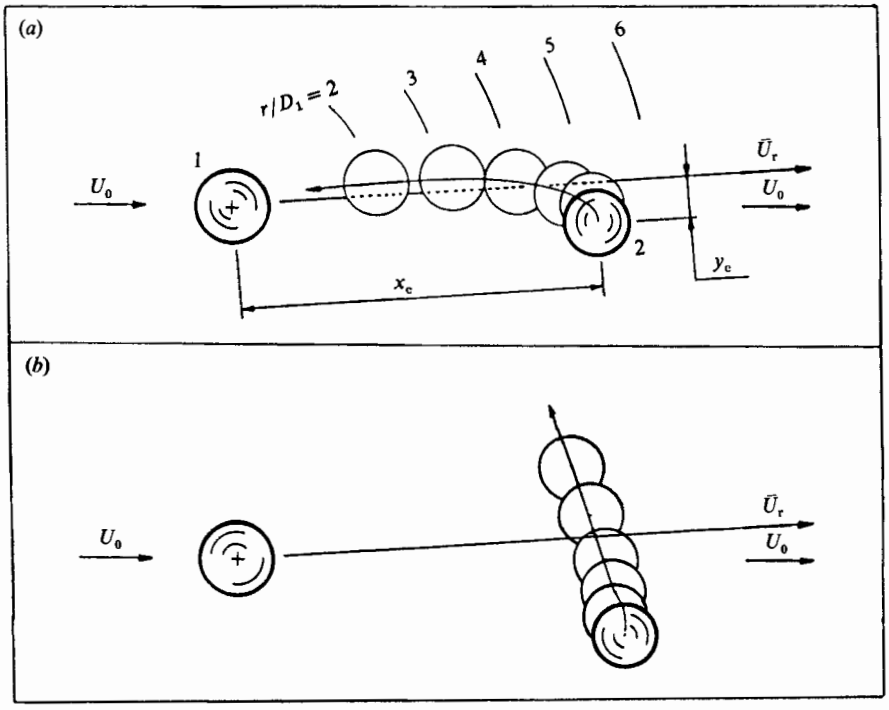


FIGURE 15. Motion of second droplet relative to first. (*a*) Capture, (*b*) escape. $U_r$ is flow velocity relative to first droplet.

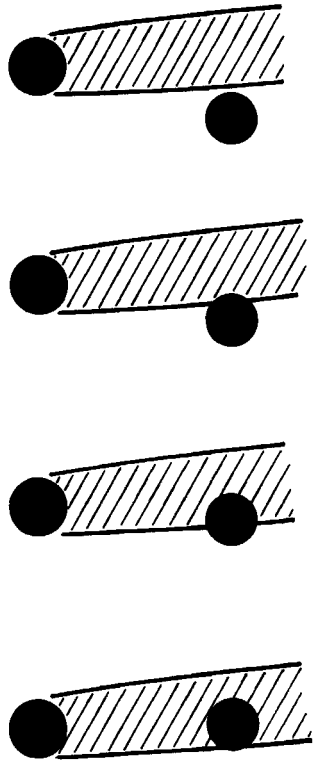

FIGURE 16. Idealized wakes behind droplets in first stream.

shaded regions behind the droplets in the first stream. These regions are drawn with an angle to the horizontal, indicating the direction of the flow relative to the droplet. In terms of this idealized picture, the interaction between droplet pairs is due to an interaction between the second droplet and the wake behind the first. This interaction must clearly result in a decrease of the drag forces on the second droplet, relative to their value for a single droplet in the same flow. It therefore became evident that one manner of quantifying the interaction was to measure fluid forces acting on the droplets, that is, measure drag coefficients. We further concluded that the drag decreases may be used to quantify the regions of interaction, e.g. the wakes behind the first droplet. Measurements of drag coefficients for the three cases mentioned earlier, made with the procedures outlined below, are shown in figures 17 and 18. Figure 17 shows the variations with time of the drag coefficient for the first droplet in the pair. Figure 18 shows the same results for the second droplet. Each figure also shows, for comparison, the steady drag. Consider the drag on the first droplet. Figure 17 clearly shows that its value for all three cases is larger than the steady drag. These trends are the same as for a single droplet in a similar flow field (Temkin & Kim 1980). Furthermore, the drag on the first droplet has approximately the same value, regardless of what happens to the second droplet. This is in contrast to the drag on the second droplet, whose value strongly depends on the interaction.

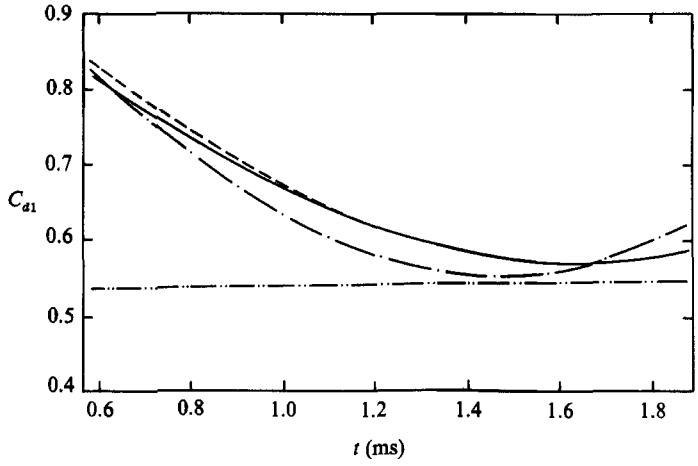


FIGURE 17. Drag coefficient of first droplet *vs.* time: —·—, 'escape'; —, collision; ---, 'retarded'; —··—, steady drag.

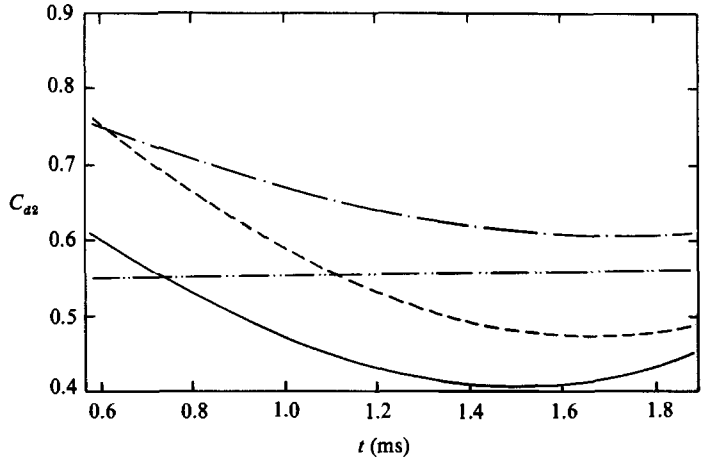


FIGURE 18. Drag coefficient of second droplet *vs.* time: —·—, 'escape'; —, collision; ---, 'retarded'; —··—, steady drag.

## 4. Data reduction and analysis

Because our experiments were performed with double droplet streams, photographic records of the motion of at least 200 droplet pairs were obtained. To provide data for a single pair that is useful for analysis, an average of about 40 $(x,y)$ positions have to be carefully selected and measured by eye from dark-field negatives, of the type shown in figure 8, using a high magnification projector as described earlier. We deemed it unnecessary to reduce the data for every pair available. Instead, we selected an average of 4–5 pairs per experiment, giving a total of 64 droplet pairs for which the data were reduced. Seven pairs out of these 64 produced data that had to be discarded because they had very large estimated errors. Basic information on the remaining 57 pairs is given in table 2. In this table, $U_0$ represents the air velocity behind the shock front, $D_{av}$ is the average droplet diameter

| $U_0$(m/s) | $D_{av}$(μm) | $Re_{max}$ | $We_{max}$ | Number of pairs |
|---|---|---|---|---|
| 7.2 | 275 | 135 | 0.15 | 32 |
| 12.1 | 278 | 227 | 0.37 | 3 |
| 17.3 | 265 | 307 | 0.71 | 4 |
| 21.7 | 276 | 408 | 1.20 | 4 |
| 27.1 | 268 | 496 | 1.81 | 4 |
| 31.2 | 268 | 578 | 2.48 | 10 |

TABLE 2. Basic characteristics of 57 pairs of droplets

in the pair. This average is used to define the Reynolds and Weber numbers, as follows:

$$Re = \frac{\rho U_r D_{av}}{\mu}, \tag{1}$$

$$We = \frac{\rho D_{av} U_r^2}{2\sigma}. \tag{2}$$

In these equations, $\rho$ and $\mu$ are the density and viscosity of the air around the droplet, and $\sigma$ is the surface-tension coefficient for the liquid–air interface. The quantity $U_r$ in these definitions is the magnitude of relative velocity $\boldsymbol{U}_r$ between fluid, $\boldsymbol{U}_f$ and droplet, $\boldsymbol{U}_p$. That is,

$$U_r = |\boldsymbol{U}_r| = |\boldsymbol{U}_f - \boldsymbol{U}_p|. \tag{3}$$

For planar motion, such as that taking place in these experiments, $U_r$ is given by

$$U_r = [(U_0 - u_p)^2 + (v_f - v_p)^2]^{\frac{1}{2}}, \tag{4}$$

where $u_p$ and $v_p$ are the horizontal and vertical components of the droplet velocity, and $v_f$ is the vertical fluid velocity at the location of the droplet, a quantity that will be discussed later. Thus, the maximum relative velocity occurs immediately after the passage of the shock front, when $\boldsymbol{U}_p$ has a negligible component along the direction of the flow. It is this maximum velocity that was used in computing the maximum Reynolds and Weber numbers listed in the table.

As table 2 indicates, the bulk of the data refers to droplet pairs having a maximum Weber number of 0.15. We chose this maximum value for most of our experiments because droplet deformation due to the imposed flow is then negligible. The data reported here are limited to these 32 non-deforming droplet pairs. The remaining 25 droplet pairs include deformation effects in varying amounts, but not resulting in breakup. Such data have been used by us to obtain drag coefficient information for deforming droplets. Those results are available in Ecker (1985), and will be reported in the future.

Let us now return to the question of trajectories. Once a droplet pair has been identified, the positions of both droplets in the pair are obtained at several instants by direct measurements of the bright spots on the dark-field negatives, using carefully obtained calibrations for the overall optical magnification. As implied earlier, the droplets move in a plane parallel to the axis of the tube, so that the displacement vector of the droplets has only two components. We shall use two coordinate systems to describe the motion. In the first, we take the $X$-axis to be aligned with the direction of the incoming flow, as shown in figure 19. We have fitted

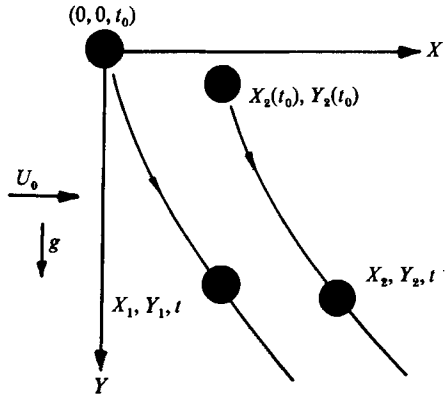


FIGURE 19. Laboratory system of coordinates.

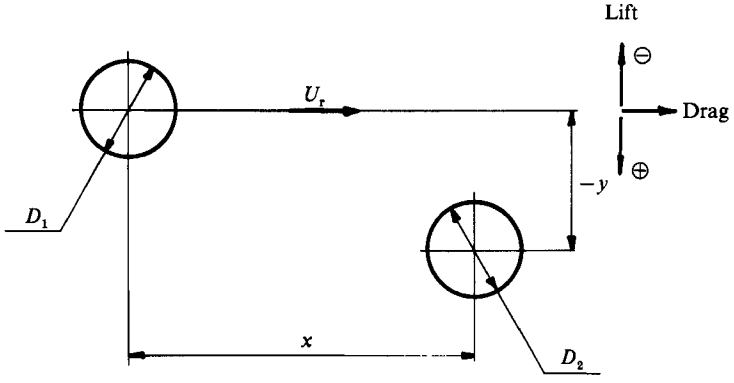


FIGURE 20. Rotated coordinate system fixed on first droplet.

these displacements with time polynomials of orders 3, 4, and 5, and determined the estimated errors produced by each. (For details and tabular comparisons, see Ecker 1985.) For the case of the non-deforming droplets reported here, we have determined that fourth-order polynomials in time produce the most accurate drag results. Thus, the horizontal and vertical displacements for a given droplet are given by expressions of the form

$$X_p = a_0 + a_1 t + a_2 t^2 + a_3 t^3 + a_4 t^4, \tag{5}$$

$$Y_p = b_0 + b_1 t + b_2 t^2 + b_3 t^3 + b_4 t^4, \tag{6}$$

where the coefficients $a_n$ and $b_n$ are chosen so as to minimize the error of the fit. Standard deviations for the displacement polynomials are also given by Ecker for each experiment. We also fitted out data with polynomials of degrees 3 and 5 and, as explained later, used these fits to ascertain the accuracy of the drag data evaluated with fourth-order polynomials.

Because the relative velocity vector is generally not aligned with the direction of the incoming flow, it is also convenient to use the coordinate system $x, y$ shown in figure 20. This system is obtained from the first by rotation through an angle $\alpha$, given by

$$\tan\alpha = \frac{v_f - v_p}{U_0 - u_p}. \tag{7}$$

This angle remains nearly constant during each experiment.

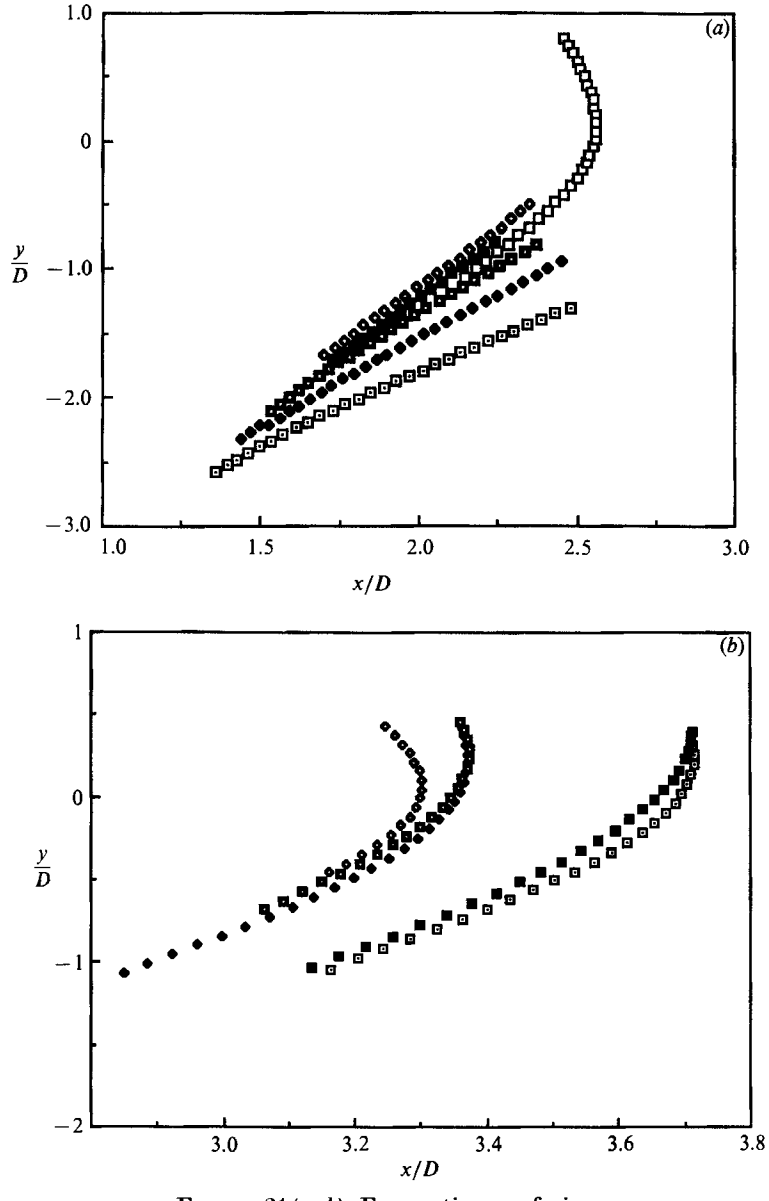


FIGURE 21 (*a*, *b*). For caption see facing page.

In figure 12, we showed some trajectories of droplet pairs in a laboratory frame of reference. It is convenient to plot the trajectories of the second droplet with respect to the first, using as horizontal axis the instantaneous direction of the relative velocity vector. Figure 21 (*a*–*d*) shows several such trajectories for a wide range of $x/D$. The remaining trajectories tend to overlap those shown in the figure. The instantaneous direction of the wake is given by those points having $y/D = 0$. In most of the trajectories shown, the second droplet starts somewhere below the axis, and terminates its motions at different locations which depend on a variety of factors such as initial location and vertical momentum. In one or two cases, the range of $y/D$ exceeded those given in the figure. In such cases, the second droplet interacted

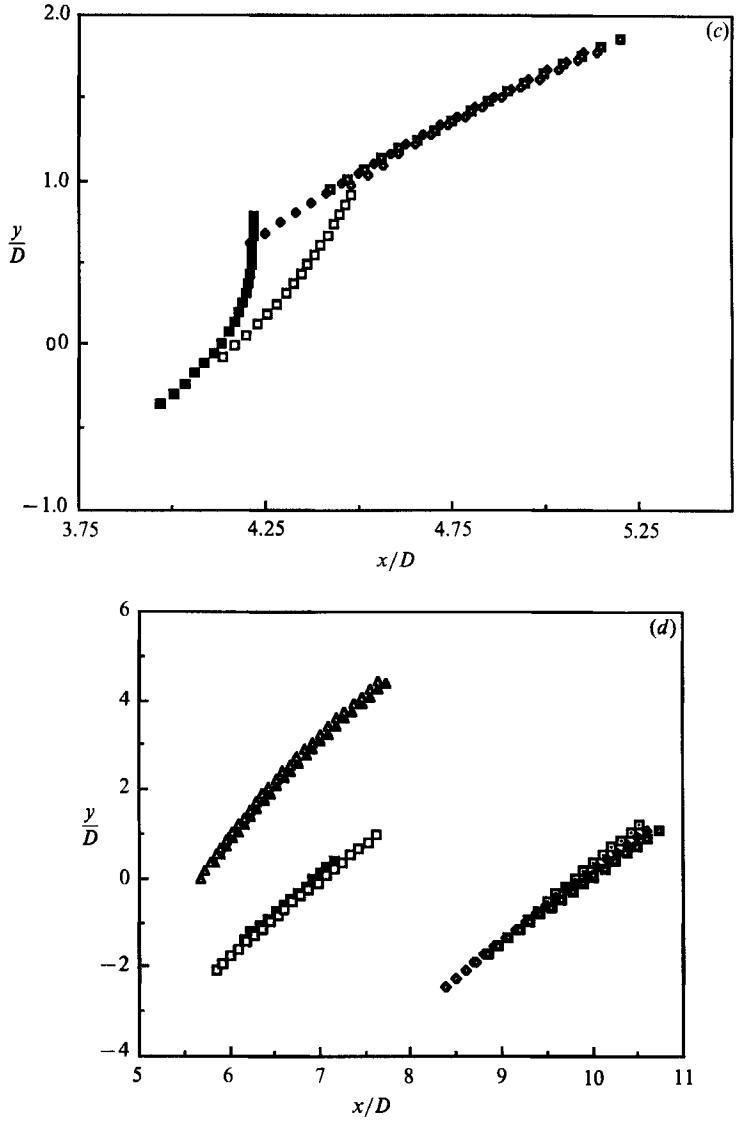


FIGURE 21. Trajectories of second droplet relative to first (*a*) $1.5 < x/D < 2.6$; (*b*) $2.8 < x/D < 3.8$; (*c*) $4 < x/D < 5.3$; (*d*) $5.5 < x/D < 10.5$.

with its main companion in the initial pair, and with the droplet above it; this will be considered later. It should also be added that, as may be expected, the effects of the interactions are more pronounced at low values of $x/D$ (figure 21*a*, *b*) than at larger values.

Consider now the forces on the droplets. The equation of motion for each is

$$m_{\mathrm{p}} \frac{\mathrm{d}\boldsymbol{U}_{\mathrm{p}}}{\mathrm{d}t} = \boldsymbol{F}_{\mathrm{f}} + \boldsymbol{F}_{\mathrm{b}}, \tag{8}$$

where $m_{\mathrm{p}}$ is the mass of a droplet, $\boldsymbol{U}_{\mathrm{p}}$ is its velocity, and $\boldsymbol{F}_{\mathrm{f}}$ and $\boldsymbol{F}_{\mathrm{b}}$ are, respectively, the fluid and body forces acting on it. As gravity is the only body force acting on the droplets, we have $\boldsymbol{F}_{\mathrm{b}} = m_{\mathrm{p}}\boldsymbol{g}$. The fluid forces are usually expressed in terms of a drag

coefficient $C_d$. This can be easily expressed in terms of quantities referred to the rotated system of coordinates, because the drag acts on the direction of $\boldsymbol{U}_r$. Thus

$$F_f = \tfrac{1}{8} C_d \pi D^2 \rho |\boldsymbol{U}_f - \boldsymbol{U}_p| \boldsymbol{U}_r \cdot \boldsymbol{e}_x \tag{9}$$

where $\boldsymbol{e}_x$ is a unity vector along the $x$-axis. In an experiment of this type, where the imposed flow filed does not reverse direction, $\boldsymbol{e}_x$ always points in the direction of $\boldsymbol{U}_r$. Thus,

$$F_f = \tfrac{1}{8} C_d \pi D^2 \rho U_r^2. \tag{10}$$

Taking the dot product of (8) with a unit vector along the direction of the relative velocity vector, we obtain

$$C_d = \frac{4}{3} \frac{\rho_p}{\rho} \frac{D}{U_r^2} (a_x + g \sin \alpha), \tag{11}$$

where $a_x = \boldsymbol{e}_x \cdot (\mathrm{d}\boldsymbol{U}_p/\mathrm{d}t)$. However, because our displacement measurements are along the unrotated axis, $X, Y$, it is convenient to write $C_d$ in terms of the acceleration components along those axis. Thus,

$$C_d = \frac{4}{3} \frac{\rho_p}{\rho} \frac{D}{U_r^2} \left[ \frac{\mathrm{d}u_p}{\mathrm{d}t} \cos \alpha + \left( g - \frac{\mathrm{d}v_p}{\mathrm{d}t} \right) \sin \alpha \right]. \tag{12}$$

Similarly, the lift coefficient, $C_L$, is given by

$$C_L = \frac{4}{3} \frac{\rho_p}{\rho} \frac{D}{U_r^2} \left[ \frac{\mathrm{d}u_p}{\mathrm{d}t} \sin \alpha - \left( g - \frac{\mathrm{d}v_p}{\mathrm{d}t} \right) \cos \alpha \right]. \tag{13}$$

The acceleration components appearing on the right-hand side of these equations are obtained from the displacement polynomials given earlier. As these equations show, the angle $\alpha$ and the relative velocity $U_r$ are needed to obtain $C_d$. Both quantities require the two components of the fluid and droplet velocities. The two components of the droplet velocity may be obtained from the displacement polynomials, and $U_0$, the convective horizontal velocity behind the shock front, may be determined from pressure measurements in conjunction with the shock equations. The remaining component, $v_f$, requires some assumptions, as it cannot be evaluated experimentally.

### 4.1 *Vertical component of fluid velocity*

We have defined $\boldsymbol{U}_f$ as the velocity that the fluid would have at the location of the droplet in the absence of the droplet. Thus, if we had a single droplet falling in a gas under the effects of gravity, that velocity component would be zero. In the present experiments, however, the vertical velocity at the location of any given droplet would not be zero because previous droplets in the stream may have passed that location, inducing a vertical velocity component. In our previous work (Temkin & Kim 1980), which dealt with single streams, the problem was resolved as follows. First, we argued that for the conditions of those experiments, the droplets would not be subject to lifting forces. That is, we assumed that a single droplet moving under the effects of the imposed flow would be exposed to nearly equal pressures on both its upper and lower surfaces, thereby producing no lift. This assumption then enabled us to obtain $v_f$ from the vertical component of the droplet's equation of motion.

To ascertain the implications of that assumption, we have re-evaluated Kim's (1977) drag-coefficient data, using, in addition to the zero lift, two other methods to evaluate $v_f$, each based on different assumptions. Both of these methods used fourth-order polynomials, instead of the third-order used in the earlier work. In one of the

| Exp. no. | $D$ (μm) | $U_0$ (m/s) | $C_L = 0$ | | | $v_f = 0$ and boundary layer | | |
|---|---|---|---|---|---|---|---|---|
| | | | $Re$ | $v_f$ | $C_d$ | $Re$ | $C_L/C_d$ | $C_d$ |
| 2093 | 87 | 9.9 | 40 | 0.94 | 2.39 | 44 | 0.14 | 2.14 |
| 2064 | 87 | 13.5 | 51 | 0.79 | 1.94 | 54 | 0.10 | 1.87 |
| 3312 | 133 | 6.4 | 47 | 0.79 | 2.52 | 51 | 0.15 | 2.22 |
| 4382 | 256 | 6.3 | 109 | 0.23 | 1.20 | 114 | 0.07 | 1.14 |

TABLE 3. Kim's (1977) data with $We < 0.15$. Comparison's between methods of analysis

methods, we simply assumed that $v_f$ is zero. The other method was based on an analysis of a boundary layer produced by a continuous circular jet. This continuous, infinite jet is merely intended as a model of the droplet stream (for details of this calculation see Ecker 1985). The results of these comparisons were subdivided into two groups: Group A with $Re > 30$; and B with $Re < 30$. Table 3 shows some data from Group A, as Group B is not relevant to the data reported here. As the table indicates, the boundary-layer method and the zero-vertical-velocity method basically yield almost the same drag-coefficient results for this group. The small differences are in fact comparable with the estimated errors in measuring $C_d$. (For Group B, containing data for $Re < 30$, the boundary-layer method produces results that are somewhere in the middle of the other two methods.)

On the basis of this comparison, we have selected the second method for our computations. That is, we have assumed that the vertical fluid velocity is zero. This assumption results in similar errors to the other methods, and has the advantage over them of not forcing the lift to vanish. This is important to the present experiments where one droplet is moving in the vicinity of the wake produced by the other, a situation where there may be considerable lift.

### 4.2. *Drag measurements*

One by-product of this comparison is that a method was developed to estimate the accuracy of the second derivatives of the displacement polynomials. In effect what was done for each experiment was to compute drag coefficients using polynomials of order 3, 4 and 5. Data were deemed to be inaccurate if the order-4 polynomials yielded results that did not agree to better that 5% with either the order-3 or order-5 polynomials. Of the 32 no-deformation pairs, 26 satisfied this requirement. As anticipated, even in the acceptable cases, there are points having estimated errors larger than 5%, and these are found during the initial or final times. The reason for this is that those points are associated with the extreme points in the displacement polynomials. Thus, typically, the first and last 5–6 points of a given experimental run had excessive errors and were therefore discarded. (An example of the interpolated and derived data is shown in Appendix B.)

Now, consider either one of the droplets in a pair. In the absence of any interaction effects, the drag force acting on it would be given by

$$F_f = \tfrac{1}{8} C_{d\infty} \pi D^2 \rho U_r^2, \tag{14}$$

where the symbol $C_{d\infty}$ is meant to represent the drag in the absence of other droplets. As a result of the interaction, the drag force is changed to some other value, say $f_f$, and we have argued that the changes are due to a wake region, that is, to a change in $U_r$, relative to the unbounded value. Because the relative velocity in this wake

region cannot be measured in our experiments, we quantify the wake by defining an effective drag coefficient, $C_{de}$, such that

$$f_t = \tfrac{1}{8} C_{de} \pi D^2 \rho U_r^2. \tag{15}$$

To quantify the interaction, we use the following non-dimensional function:

$$g(C_d) = \frac{f_t - F_t}{F_t} = -\frac{C_{d\infty} - C_{de}}{C_{d\infty}}. \tag{16}$$

Now, a measurement of the effective drag, alone, cannot quantify the wake. Other variables play an important role, such as the Reynolds number, the location of the second droplet relative to the first, and the unsteadiness of the flow. For the following reasons, we have ignored the variations of the Reynolds number, and have disregarded the effects of flow unsteadiness on the drag coefficient of an isolated droplet.

The Reynolds number was based on the incoming free-stream velocity and on an average diameter for a droplet pair. For the non-deforming droplets under consideration, it had a maximum value which was about 135 for all of these pairs. Typically, during an experiment it would decrease by less than 10%. Although this is not negligible, it is relatively small so we may regard the Reynolds number as a constant during each experiment. Because of this, we decided to use steady drag data for $C_{d\infty}$ even though, for the conditions of our experiments, the drag is larger than the steady drag (Temkin & Kim 1980). The effect of scaling the data with the steady drag rather than with the unsteady, is to underestimate drag changes. However, in the Reynolds-number region of interest to these experiments, the differences between steady and unsteady drag are small.

As may be expected, the most important parameter in determining drag changes is the instantaneous location of the second droplet, relative to the first. This location changes during an experiment, in a manner that varies significantly from pair to pair as shown earlier. The changes in drag coefficients are clearest for those cases where the horizontal separation between first and second droplets did not change significantly during the experiment. Figure 22 shows such a case [Experiment 37/s8/p4]. As the figure shows, the second droplet begins to feel the effects of the wake of the first at a vertical distance that is of the order of one droplet diameter. As the droplet continues its upward motion, the fluid forces on it continue to decrease until a minimum is reached in the vicinity of $y/D = 0$, the axis of the wake. Beyond that point, the drag on the second droplet increases, and achieves its 'free stream' value at a vertical distance that is also of the order of one droplet diameter.

Several points can be made on the basis of this figure. First, and as already indicated, the interaction is due to the wake behind the first droplet. Second, at least for this horizontal separation, the first droplet is not felt by the second at vertical distances larger than about one diameter. Third, the changes in drag are very significant for vertical distances smaller than about one droplet radius. Fourth, the drag changes on the first droplet in the pair are small throughout the experiment. They are, in fact, slightly smaller than the maximum error allowed. We shall therefore neglect them and concentrate on the data for the second droplet in the pair.

In some cases, as mentioned earlier, the second droplet interacts with two consecutive droplets in the first stream during an experiment (such secondary interactions are indeed likely to occur in every experiment, but they occur outside

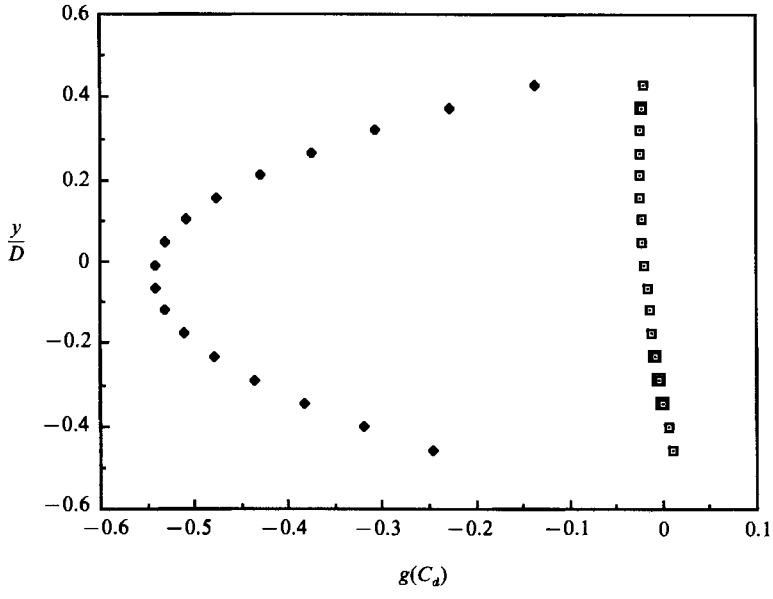


FIGURE 22. Drag changes in one experiment: $x/D \approx 3.1$; ⊡, first droplet; ◆, second droplet.

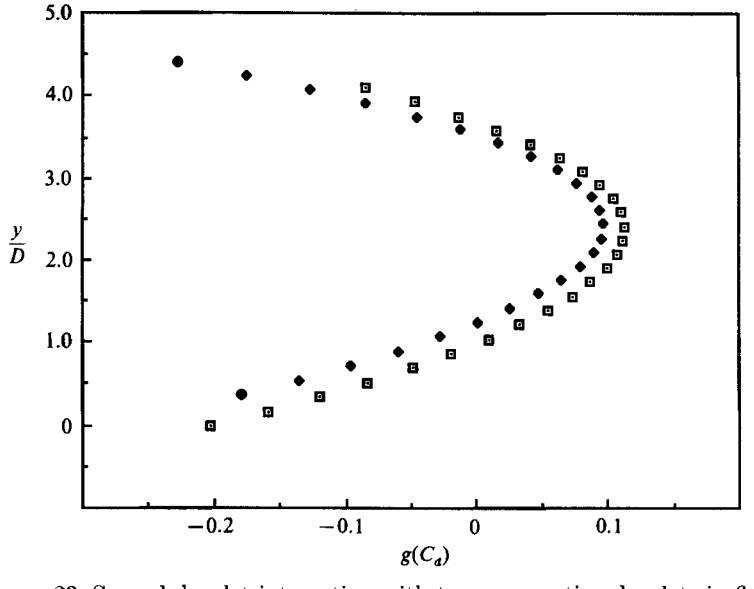


FIGURE 23. Second droplet interaction with two consecutive droplets in first stream.

the observation region). These secondary interactions occur when the second droplet penetrates the wake of a second droplet in the first stream, that is, when its vertical distance from the axis of the first droplet exceeds 3–5 droplet diameters. In such cases, the drag-reduction curve for the corresponding trajectory may show two regions with significant decreases, as indicated in the cases shown in figure 23. In what follows, we concentrate on vertical distances smaller than 2 diameters. Secondary interactions are not detected at such distances.

Figure 24 shows the drag changes on the second droplet for all of our small-error

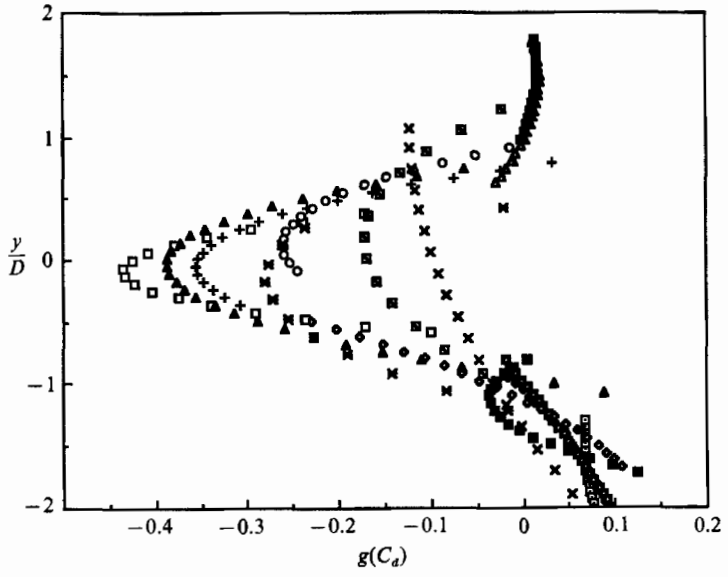


FIGURE 24. Drag-coefficient changes for second droplet.

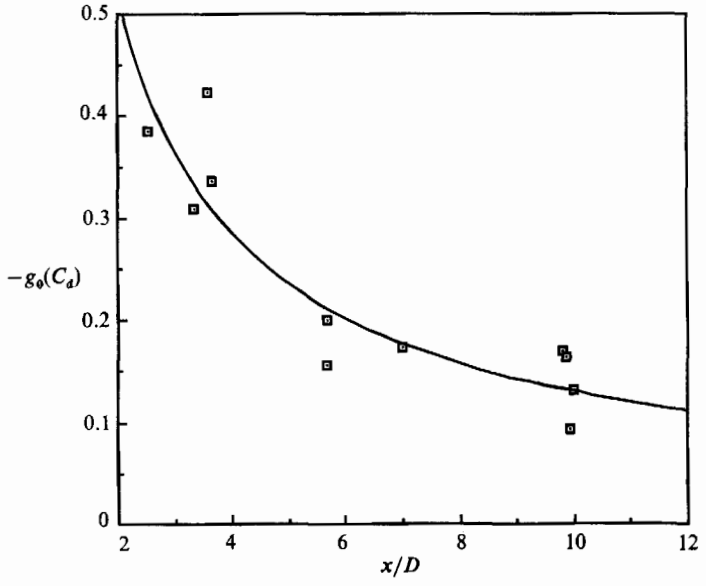


FIGURE 25. Axial-drag-coefficient changes.

pairs. While bell-shaped profiles for the drag changes are apparent, the figure is slightly misleading because it shows all of the data. That is, it combines data from droplets at *different* horizontal distances from the first. The fact that a trend can be discerned in the graph is simply an indication that drag changes along the horizontal are comparatively slow in the range observed. This is, whereas along the vertical the quantity $g(C_d)$changes from 0 to about 0.5 in less than one diameter, it takes more than 10 diameters to change it by a comparable amount along the horizontal. This is shown in figure 25, which displays the changes of $-g(C_d)$ with non-dimensional

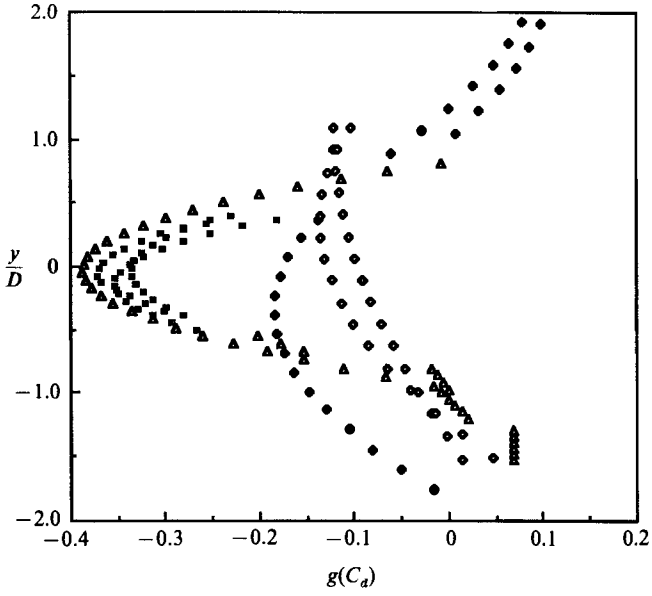


FIGURE 26. Drag reduction for selected ranges of $x/D$: △, $x/D = 2.4$; ■, 3.6; ◆, 6.5; ◇, 9.5.

horizontal distance for those data having $y/D = 0$. The solid line in the figure is a least-square fit to the data, and it is given by

$$-g_0(C_d) = A\, e^{-B(x/D)}, \tag{17}$$

where $A = 0.595$ and $B = 0.145$.

Because of this relatively weak dependence on the horizontal distances, we may divide the data into groups having horizontal separations that are only roughly equal, and plot for each the variations of $g(C_d)$as a function of $y/D$. Figure 26 shows four such groups, covering the ranges of $x/D$ between 2.25 and 9. While there is considerable scatter, particularly for the group having the largest values of $x/D$, where the error is larger, the curves show the trends rather clearly. Thus, the highest drag decreases as found closest to the first droplet in a narrow region near $y/D = 0$. As we move away from the first droplet, the region where changes occur widens around $y/D = 0$, but the changes decrease in magnitude, as might be expected of a wake. For a given value of $x$, the drag reduction depends on $y$ as $\exp[-C(y/D)^2]$, where $C = 2.253$. Thus,

$$g(C_d) = g_0(C_d)\, e^{-C(y/D)^2}. \tag{18}$$

The standard deviations for $A$, $B$ and $C$ are 0.047, 0.022, and 0.149, respectively. The trends may be collapsed into a single pattern, by scaling the values of $g(C_d)$ with those occurring at $y/D = 0$. Thus,

$$G(C_d) = -\frac{g(C_d)}{g_0(C_d)}, \tag{19}$$

where $g_0(C_d)$ is given by (17). The results of the scaling are shown in figure 27. This figure includes more than 300 data points.

We may use the above fit for the drag-reduction data to get an idea of the average velocity profiles in the wake. We do this by defining an effective relative velocity in a manner similar to that used earlier to define an effective drag coefficient. Thus, if

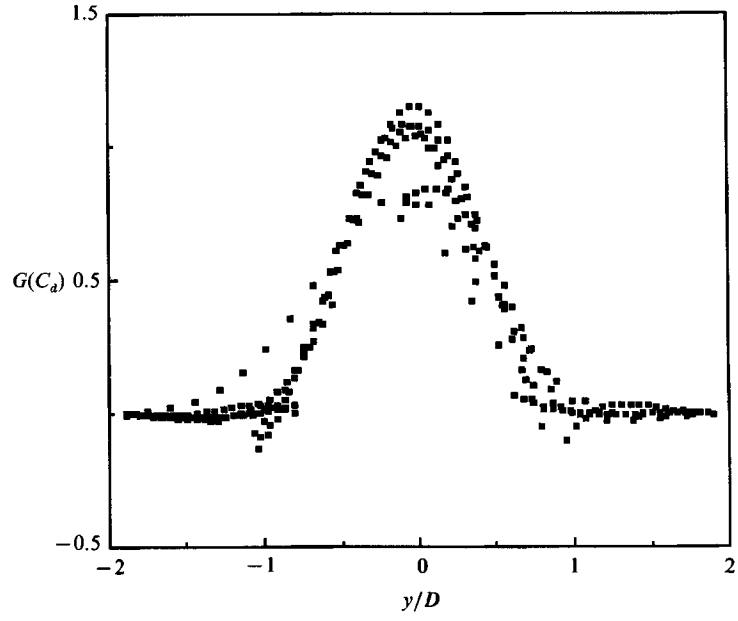


FIGURE 27. Scaled drag-reduction data: $G(C_d) = -g(C_d)/g_0(C_d)$.

$U_{re}$ is a measure of the effective relative velocity, we may write $C_{de}\, U_r^2 = C_{d\infty}\, U_{re}^2$ or, on using (16),

$$\frac{U_{re}}{U_r} = [1+g(C_d)]^{\frac{1}{2}}. \tag{20}$$

Reference to (18) shows that the velocity ratio approaches unity as either $x$ or $y$ are increased. Equations (18)–(20) can also be used to get an idea of the size of the region where the first droplet has an influence on the second droplet. Thus, if we define that region as being that where the velocity ratio is not larger than 0.97, then the surface of influence is limited by a paraboloid of revolution given by

$$\frac{x}{D} = \frac{C}{B}\left[1-\left(\frac{y}{D}\right)^2\right], \tag{21}$$

where $B(=0.145)$ and $C(=2.253)$ are the fit coefficients given earlier. As this equation shows, the region of influence extends to more than 15 diameters in the axial direction.

On the basis of these results we may envision each of the droplets as endowed with such a region of influence, as shown in figure 16 for the droplets in the first stream, except that the length is finite. Droplets in the second stream are also followed by such regions, but these are not drawn in the figure.

## 5. Conclusions

We have considered the interaction between two droplets in a shock-wave flow field. One of the main conclusions arrived on the basis of this study is that the upstream droplet is not significantly affected by the interaction, and that the most significant effect on the downstream droplet is due to a narrow paraboloid wake which is formed in the lee side of the upstream droplet. Roughly speaking, this

paraboloid has a width of one droplet diameter and a length of 15 diameters. Other droplets penetrating this region are exposed to reducted imposed velocities, resulting in reduced drag forces. The drag reduction experienced by the downstream droplet appears to be well described by a normal distribution.

An important question not answered by these experiments is how does the interaction region depend on the Reynolds number. It is clear, however, that the interaction ought to exist so long as a wake is formed, and this will occur so long as the Reynolds number is larger than 10–20. Also, on physical grounds we expect that the length of the region of interaction decreases with the Reynolds number, although we are unable to quantify the decrease. Nevertheless, to the extent that the ranges of our parameters apply to other situations, we may model droplet interactions in clouds by endowing the lee side of each droplet in the cloud with a cigar-shaped wake that is aligned with the direction of the local velocity relative to each droplet. Outside these wakes, the fluid velocity corresponds to that in the free stream. Although this model of the interaction region is crude in comparison to the real velocity distribution in the wake of the upstream droplets, it nevertheless provides a basis for the study of multiparticle systems in finite-Reynolds-number flows.

This research was supported in part by a grant from the Victor and Erna Hasselblad Foundation.

## Appendix A. Droplet diameters and separations in μm for experiment 37/s10.

| | First stream | | Second stream | |
|---|---|---|---|---|
| Drop no. | $D_{hor}$ | $D_{ver}$ | $D_{hor}$ | $D_{ver}$ |
| 1 | 282.4 | 288.0 | 265.2 | 265.2 |
| 2 | 279.9 | 279.9 | 266.2 | 266.2 |
| 3 | 280.4 | 287.0 | 260.1 | 263.1 |
| 4 | 280.4 | 284.5 | 266.2 | 265.2 |
| 5 | — | — | 267.2 | 259.6 |
| $D$ | 280.8 | 284.7 | 264.8 | 264.6 |
| $\sigma(D)$ | 1.1 | 3.8 | 2.6 | 2.9 |
| $L_{0-1}$ | 1205.0 | | 1110.0 | |
| $L_{1-2}$ | 1168.9 | | 1139.4 | |
| $L_{2-3}$ | 1280.7 | | 1153.2 | |
| $L_{3-4}$ | 1208.5 | | 1142.0 | |
| $L_{4-5}$ | — | | 1113.5 | |
| $L$ | 1215.8 | | 1190.3 | |
| $\sigma(L)$ | 27.4 | | 31.6 | |

## Appendix B. Measured (bold face) and interpolated data for second droplet in pair No. 4. Experiment 37/s10

| Time (μs) | $X_p$ (μm) | $Y_p$ (μm) | $U_p$ (m/s) | $V_p$ (m/s) | $A_x$ (m/s²) | $A_y$ (m/s²) | $C_{ds}$ | $C_d$ | $-g(C_d)$ % | $C_L/C_d$ | $x/D_{av}$ | $y/D_{av}$ |
|---|---|---|---|---|---|---|---|---|---|---|---|---|
| 0 | 0.0 | 3562.1 | 0.015 | 2.255 | 227.9 | −80.4 | 0.953 | 1.280 | 34.3 | −0.07 | 1.549 | −2.077 |
| 120 | | | 0.042 | 2.246 | 220.7 | −73.0 | 0.955 | 1.242 | 30.0 | −0.05 | 1.581 | −2.012 |
| 240 | | | 0.068 | 2.238 | 213.9 | −66.2 | 0.957 | 1.206 | 26.0 | −0.03 | 1.613 | −1.949 |
| 360 | | | 0.093 | 2.230 | 207.5 | −60.0 | 0.958 | 1.172 | 22.3 | −0.02 | 1.644 | −1.887 |
| 480 | 20.8 | 4717.3 | 0.117 | 2.223 | 201.5 | −54.3 | 0.960 | 1.140 | 18.7 | 0.00 | 1.674 | −1.827 |
| 597 | | | 0.141 | 2.217 | 196.0 | −49.3 | 0.962 | 1.110 | 15.5 | 0.02 | 1.704 | −1.769 |
| 713 | | | 0.163 | 2.212 | 190.9 | −44.9 | 0.963 | 1.083 | 12.5 | 0.03 | 1.733 | −1.769 |
| 830 | | | 0.185 | 2.207 | 186.0 | −41.0 | 0.965 | 1.058 | 9.7 | 0.04 | 1.762 | −1.655 |
| 946 | 89.4 | 5805.9 | 0.207 | 2.202 | 181.6 | −37.6 | 0.966 | 1.036 | 7.2 | 0.05 | 1.792 | −1.599 |
| 1063 | | | 0.228 | 2.198 | 177.5 | −34.8 | 0.967 | 1.015 | 5.0 | 0.06 | 1.821 | −1.543 |
| 1179 | | | 0.248 | 2.194 | 173.8 | −32.6 | 0.969 | 0.997 | 3.0 | 0.07 | 1.851 | −1.488 |
| 1296 | | | 0.268 | 2.190 | 170.3 | −30.8 | 0.970 | 0.982 | 1.2 | 0.08 | 1.881 | −1.432 |
| 1412 | 190.0 | 6905.2 | 0.288 | 2.187 | 167.3 | −29.6 | 0.971 | 0.969 | −0.3 | 0.08 | 1.912 | −1.376 |
| 1529 | | | 0.307 | 2.184 | 164.6 | −28.9 | 0.973 | 0.958 | −1.5 | 0.08 | 1.943 | −1.320 |
| 1645 | | | 0.326 | 2.180 | 162.2 | −28.8 | 0.974 | 0.950 | −2.4 | 0.08 | 1.974 | −1.264 |
| 1762 | | | 0.345 | 2.177 | 160.2 | −29.2 | 0.975 | 0.945 | −3.1 | 0.07 | 2.006 | −1.207 |
| 1878 | 329.2 | 7997.4 | 0.363 | 2.173 | 158.6 | −30.2 | 0.977 | 0.943 | −3.5 | 0.07 | 2.038 | −1.151 |
| 1995 | | | 0.382 | 2.170 | 157.3 | −31.7 | 0.978 | 0.943 | −3.6 | 0.05 | 2.071 | −1.093 |
| 2111 | | | 0.400 | 2.166 | 156.3 | −33.7 | 0.979 | 0.946 | −3.4 | 0.04 | 2.104 | −1.035 |
| 2228 | | | 0.418 | 2.162 | 155.7 | −36.3 | 0.980 | 0.952 | −2.8 | 0.03 | 2.138 | −0.977 |
| 2344 | 502.9 | 9067.8 | 0.436 | 2.158 | 155.4 | −39.4 | 0.982 | 0.962 | −2.0 | 0.01 | 2.172 | −0.918 |
| 2461 | | | 0.454 | 2.153 | 155.5 | −43.0 | 0.983 | 0.974 | −0.9 | −0.01 | 2.206 | −0.859 |
| 2577 | | | 0.473 | 2.147 | 156.0 | −47.2 | 0.984 | 0.989 | 0.5 | −0.04 | 2.240 | −0.799 |
| 2694 | | | 0.491 | 2.142 | 156.7 | −51.9 | 0.986 | 1.008 | 2.3 | −0.06 | 2.274 | −0.739 |
| 2810 | 708.7 | 10149.8 | 0.509 | 2.135 | 157.9 | −57.1 | 0.987 | 1.030 | 4.4 | −0.09 | 2.308 | −0.678 |
| 2927 | | | 0.528 | 2.128 | 159.4 | −63.0 | 0.988 | 1.055 | 6.8 | −0.12 | 2.342 | −0.617 |
| 3043 | | | 0.546 | 2.121 | 161.2 | −69.3 | 0.990 | 1.084 | 9.5 | −0.14 | 2.376 | −0.556 |
| 3160 | | | 0.565 | 2.112 | 163.4 | −76.2 | 0.991 | 1.116 | 12.6 | −0.17 | 2.410 | −0.495 |
| 3276 | 950.5 | 11210.5 | 0.584 | 2.103 | 165.9 | −83.5 | 0.993 | 1.152 | 16.0 | −0.20 | 2.442 | −0.434 |

## REFERENCES


DREYFUSS, D. & TEMKIN, S. 1983 Charge separation during rupture of small water droplets in transient flows: Shock tube measurements and application to lightning. *J. Geophys. Res.* **88**, 10993–10998.

ECKER, G. Z. 1985 Interaction of droplet pairs in weak shock wave induced unsteady flows. Ph.D. thesis, Rutgers University.

GOYER, G. 1965*a* Effects of lightning on hydrometeors. *Nature* **206**, 1203–1209.

GOYER, G. 1965*b* Mechanical effects of a simulated lightning discharge on the water droplets of 'Old Faithful' geyser. *Nature* **206**, 1302–1309.

KIM, S. S. 1977 An experimental study of droplet response to weak shock waves. Ph.D. thesis, Rutgers University.

REICHMAN, J. M. & TEMKIN, S. 1974 A study of the deformation and breakup of accelerating water droplets. *First Intl. Symp. on Drops and Bubbles, Pasadena*, pp. 446–464.

TEMKIN, S. 1969 Cloud droplet collisions induced by thunder. *J. Atmos. Sci.* **26**, 776.

TEMKIN, S. 1970 Droplet agglomeration in a shock wave flowfield, *Phys. Fluids* **11**, 1639–1641.

TEMKIN, S. 1972 On the response of a sphere to an acoustic pulse. *J. Fluid Mech.* **54**, 339–349.

TEMKIN, S. & KIM, S. S. 1980 Droplet motion induced by weak shock waves. *J. Fluid Mech.* **96**, 133–157.

TEMKIN, S. & MEHTA, H. K. 1982 Droplet drag in an accelerating and decelerating flow. *J. Fluid Mech.* **116**, 297–313.

WOODS, J. D. 1964 The wake capture of water drops in air. *Q. J. R. Met. Soc.* **91**, 35–43.